

Effect of heat treatment on mechanical property and microstructure of a powder metallurgy nickel-based superalloy



Hongyu Wu^a, Xiaoli Zhuang^b, Yan Nie^c, Yunping Li^{a,*}, Liang Jiang^{a,**}

^a State Key Laboratory for Powder Metallurgy, Powder Metallurgy Research Institute, Central South University, Changsha, 410083, China

^b State Key Laboratory for Advanced Metals and Materials, University of Science and Technology of Beijing, Beijing, 100083, China

^c Yuanmeng Precision Technology (Shenzhen) Institute, Shenzhen, China

ARTICLE INFO

Keywords:

Nickel-based superalloy
Heat treatment
Single and multi-step aging treatment
Mechanical performance
Microstructure

ABSTRACT

In this study, single and multi-step aging treatments (SAT and MAT) following a super-solvus solution treatment were employed to tailor the mechanical property of a prototypical powder metallurgy (PM) nickel-based superalloy. Vickers hardness and tensile test at room temperature were used to evaluate the mechanical properties after different heat treatments. Microstructural evolution after heat treatments and tensile tests were revealed through scanning electron microscope (SEM) and electron backscatter diffraction (EBSD) techniques. Our results show that the MAT with a stabilization at 650 °C for 24 h between the solution and aging assists to achieve the highest strength corresponding to microstructure of bimodal distribution of γ' precipitates. The associated mechanism for variation in microstructures and mechanical properties are discussed based on thermodynamic calculations and precipitation strengthening theory. In addition, an empirical relationship between Vickers hardness and tensile strength of nickel-based superalloys is examined which is believed to be assistance for rapid evaluating mechanical response of materials with different microstructures.

1. Introduction

Powder metallurgy nickel-based superalloys are widely used as turbine disc materials in aircraft engines and power generation turbines because of their excellent properties at elevated temperatures [1,2]. These alloys typically are composed of a face-centered cubic matrix (γ) and a $L1_2$ structure precipitate (γ') embedded in γ matrix [3]. The conventional heat treatment, including solution treatment and aging treatment, is considered as a powerful tool to tailor the microstructures and therefore to achieve the desired mechanical properties [3–5]. Generally speaking, the solution temperature and soaking time can be determined flexible to control the grain size [6]. Cooling rate plays an important role in tuning the features of γ' precipitates, e.g. morphology, size distribution, composition and misfit between γ matrix and γ' precipitates (the misfit changes as a function of composition of γ and γ') [7–11]. And aging temperature and time enables engineers to further improve the volume fraction and size distribution of γ' precipitates [12].

Extensive alloying elements e.g., Mo, W, Nb, Ti and Ta with different electronic structure and atomic radii compared with Ni [2] are added for solid solution strengthening and γ' precipitates strengthening

to meet the requirement of mechanical strength at elevated temperature [3,13]. These physical or structure differences in turn leads to significant interactions between each alloy element and variation in thermal properties (solid and liquid melting temperature, γ' solvus temperature) and thermodynamic behavior (nucleation, growth and coarsening behavior of γ') are expected corresponding to composition fluctuation in specific alloy. Thus a universal heat treatment strategy which could be applicable to extensive alloys is unavailable. For instance, the typical heat treatment for IN100 is consisting of sub- or super-solvus solution, stabilization at 982 °C for 1 h and aging at 732 °C for 8 h [14]. While for Udimet 720Li the maximized tensile properties appeared under the following heat treatment: sub-solvus solution at 1120 °C or 1080 °C and then aged at 760 °C for 16 h + 650 °C for 24 h [15]. The recommended heat treatment for Rene 88DT is first super-solvus solution treated and then aged at 760 °C for 8 h [16]. These investigations indicate that it is necessary to develop specific heat treatment procedure to optimize the mechanical performance when a new superalloy has been designed.

Current work focuses on the development of an appropriate heat treatment strategy for a prototypical PM nickel-based superalloy. The alloy was first super-solvus solution treated and then aged with SAT and

* Corresponding author.

** Corresponding author.

E-mail addresses: lyping@csu.edu.cn (Y. Li), liang.jiang@csu.edu.cn (L. Jiang).

Table 1

Nominal chemical composition of the nickel base superalloy in wt.%

| Ni | Co | Cr | Mo | W | Al | Ti | Nb | C | B | Zr | Hf |
|------|----|----|----|---|-----|-----|------|------|-------|------|-----|
| Bal. | 26 | 13 | 4 | 4 | 3.2 | 3.7 | 0.95 | 0.05 | 0.025 | 0.05 | 0.2 |

MAT. Corresponding mechanical responses were investigated using Vickers hardness test and tensile test at room temperature. Scanning electron microscopy (SEM) and electron backscattered diffraction (EBSD) were served to reveal the microstructural features produced under different heat treatments. Our experimental results show that the maximized mechanical performance occurs under the heat treatment consisting of super-solvus solution at 1180 °C for 40 min, stabilization at 650 °C for 24 h and aging at 760 °C for 16 h in the studied strategies. The related strengthening mechanism is discussed based on the microstructure evolution. The developed features of γ' precipitates are analyzed using precipitation kinetic simulation. In addition, an empirical law between Vickers hardness and tensile strength is examined which is expected to be assistance in fast assessing mechanical strength of nickel-based superalloys.

2. Experimental detail

The alloy used in this study is a newly developed polycrystalline nickel-based superalloy by powder metallurgy (PM) processing route. The nominal composition of this alloy is listed in Table 1. This alloy was prepared by vacuum induction melting and then argon-atomization. Powder with a size range below 74 μm was collected and filled in a stainless steel container, which was outgassed and sealed by welding for following hot isostatic pressing (HIP). The HIP process was carried out at 1170 °C and 150 MPa for 4 h. The density of the alloy after HIP was measured to be $8.22 \pm 0.01 \text{ g/cm}^3$. Specimens were produced using wire-based electrical discharge machining for the following heat treatment. The schematic of the heat treatment strategies is presented in Fig. 1 and consisted of solution treatment at 1180 °C for 40 min (step 1), stabilization at 980 °C for 1 h (step 2) or 650 °C for 24 h (step 3) and aging at 760 °C for 8 h (step 4) or 16 h (step 5), as shown in Fig. 1. All the cooling path applied for the above treatments was air cooling. The heat treatment for all specimens was operated at a tube furnace with

argon gas protection and the heating rate was 10 °C/min.

Field emission SEM (Quanta 650 FEG, FEI) was used to observe the γ' precipitates and fractography of the specimens after tensile test using the secondary electron mode. Specimens for γ' observation were polished with the standard metallurgical procedure and then etched using a $\text{H}_2\text{O}:\text{HNO}_3:\text{CH}_3\text{COOH}:\text{HF} = 33:33:33:1$ solution. EBSD technique was performed using a step size of 0.3–0.6 μm and an accelerating voltage of 20 KV to reveal the microstructure both before and after deformation. Vibration polishing was performed on specimens before deformation for EBSD observation. While electrochemically polish was applied to acquire the post mortem deformation microstructure [17]. Statistical analysis for γ' precipitates was carried out using the software ImageJ according to the method described in Ref. [18] and the reported values for volume fraction and average diameter of γ' precipitates were averaged from three measurements in each case. It should be noted that due to the resolution limitation of SEM, the quantitative information about tertiary γ' was unrepresented in this work.

Vickers hardness test at room temperature was carried out at the Buehler Micrometer 5100 hardness tester with a maximum load of 1 kg and dwell time of 15 s. Each value was obtained through averaging ten measurements.

Tensile tests were performed at room temperature using a computer-controlled tensile testing machine on as-HIPed and heat treated specimens with a constant initial strain rate of 10^{-3}s^{-1} . The dog bone-shaped tensile specimen had a gauge length of 8 mm, a width of 3 mm and a thickness of 2 mm. The surface of the tensile specimens was polished down to a 1200-grit SiC paper to remove the recast layer resulting from the wire-based electrical discharge machining process. Three tensile specimens were examined for each condition for the reproducibility.

Thermodynamic calculation for driving force and number density of γ' was performed using the Pandat software with Panprecipitation module [19].

3. Results

3.1. Mechanical properties evolution

3.1.1. Vickers hardness

The Vickers hardness values of specimens under different heat

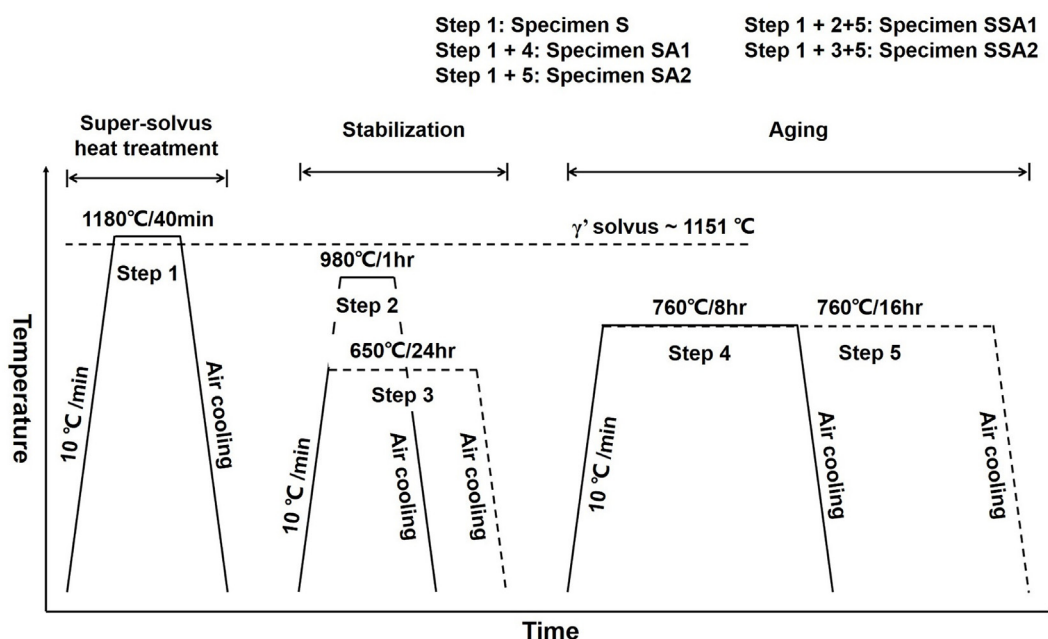


Fig. 1. Schematic showing the sequence of heat treatment procedures.

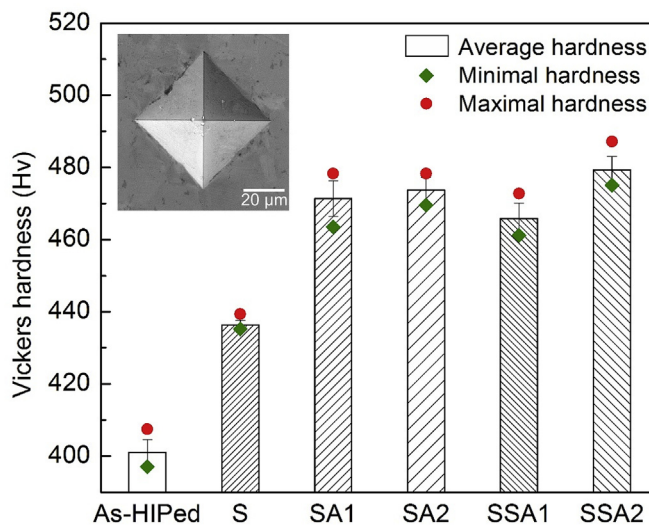


Fig. 2. Vickers hardness evolution under different heat treatments (insert a typical indentation in the as-HIPed specimen).

treatment are plotted in Fig. 2, where the insert is a typical indentation after hardness test in as-HIPed specimen. The diagonal length is about 60 μm under the load of 1 kg. It can be seen that there is a significant increase of hardness in solution treated (436 Hv) and solution + aging treated (466–479 Hv) specimens compared with the as-HIPed specimen (401 Hv). In the cases of SAT (specimens SA1 and SA2), it seems that aging longer time offers limited help for reaching a higher hardness, namely, a slight increment of 2 Hv is generated when aged additional 8 h. However, the value of hardness drops from 473 to 466 Hv for the specimen SSA1 stabilized at 980 $^{\circ}\text{C}$ for 1 h and aged at 760 $^{\circ}\text{C}$ for 16 h. In contrast, stabilization at low temperature (650 $^{\circ}\text{C}$ for 24 h) followed by the same aging makes the specimen achieve the highest hardness (479 Hv). These results clearly indicate that the solution and aging treatments play a vital role in improving the mechanical property in nickel-based superalloys.

3.1.2. Tensile property

Fig. 3 shows the tensile property obtained at room temperature of the as-HIPed and heat treated specimens. After solution and aging treatment, higher tensile strength and lower elongation are observed in all specimens. However, tensile property responses resulted by different aging treatments are not always same. For example, solution (specimen S) and aging treatment at 760 $^{\circ}\text{C}$ for 8 h (specimen SA1) make the

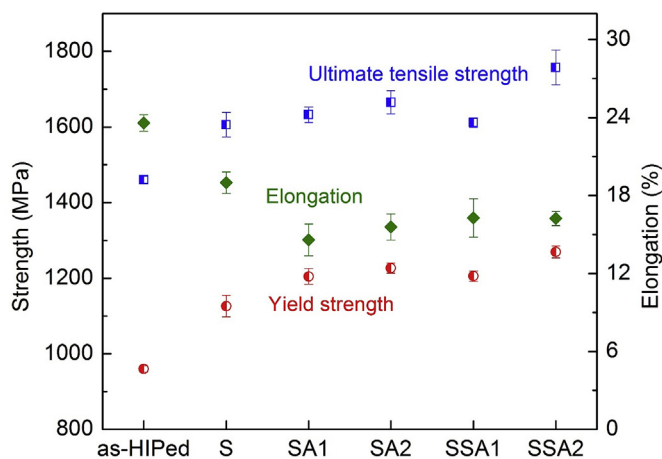


Fig. 3. The yield strength, ultimate tensile strength and total elongation of the as-HIPed and heat treated specimens.

tensile strength (both ultimate tensile strength and yield strength) increase but elongation reduce monotonically. Longer aging time (16 h, specimen SA2) or stabilized at high temperature with a short time (980 $^{\circ}\text{C}$ /1 h, specimen SSA1) achieve an increase in elongation compared with specimen SA1 while maintain the tensile strength (specimen SA2) or reduce the tensile strength slightly (for specimen SSA1) at the same time. When a lower temperature (650 $^{\circ}\text{C}$) and longer time (24 h) stabilization process is applied, the highest tensile strength (among all the aging treated specimens) is realized accompanied with an acceptable elongation. These results show the advantage of stabilization process at low temperature with a long duration in helping the alloy reach an excellent tensile property at room temperature.

3.2. Microstructural evolution

3.2.1. γ' precipitates

Fig. 4 shows the features of γ' precipitates for as-HIPed and heat treated specimens, it can be seen that heat treatment especially the solution treatment show significant impact on tuning the features of γ' precipitates. For the as-HIPed specimen, two type of γ' are observed, the butterfly-shaped secondary γ' (about 200 nm in diameter, detailed statistical analysis for the γ' will be presented in the discussion section) and small spherical tertiary γ' (< 50 nm, as indicated by yellow arrows in Fig. 4a). During the super-solvus solution treatment, γ' precipitates dissolve and then re-produce in the solution cooling process [20]. Accordingly, all the specimens after solution treatment exhibit different morphologies and size distributions compared with that in as-HIPed specimen. Fig. 4b shows the γ' precipitates of specimen S with only solution treatment applied. Compared to as-HIPed specimen, all γ' precipitates show near spherical or cubical morphology, no split of γ' precipitates are observed in this case. The size of γ' is much smaller and the number density is higher. Direct aging at 760 $^{\circ}\text{C}$ for 8 (specimen SA1) and 16 h (specimen SA2) lead to a small increase in size of γ' compared to specimen S, as shown in Fig. 4c and d, respectively. Both in these two cases, the γ' precipitates present more cuboidal morphology. The specimens underwent stabilization between solution and aging treatments show lower number density of secondary γ' precipitates than specimen SA2 (Fig. 4e and f). However, the size of γ' in specimen SSA2 is smaller than SSA1 indicating stabilization at high temperature is helpful to the growth of γ' . From the SEM image (Fig. 4f) of SSA2, very fine spherical tertiary γ' precipitates develop in the channel between secondary γ' , as indicated by yellow arrows in the insert image of Fig. 4f.

3.2.2. Grain size evolution

Fig. 5 shows the grain size evolution during different heat treatments. The as-HIPed specimen has the smallest grain size (with average diameter of 8.5 μm , see Fig. 6a), while a small increase in grain size of all specimens after solution and solution + aging treatment are observed compared with as-HIPed specimen. The average grain size of these specimens locates in the range of 9–11 μm based on the EBSD measurements (Fig. 6). The largest grain size is corresponding to the specimen SSA1, reaching an average diameter of ~ 11 μm , as evident in Figs. 5e and 6e. Interestingly, in all specimens the powder-like (or circular) grains are developed whose morphology suggests that those grains are inherited from the raw powders. In addition, all specimens show bimodal grain size distribution, i.e., some large grains (indicated by the black arrows in Fig. 6) are embraced by small ones.

3.3. Microstructural evolution upon deformation

In order to investigate the deformation details of the specimens, the cross-sectional areas near the fractured tip are examined by EBSD IPF and kernel average misorientation (KAM) maps, as shown in Fig. 7. Here, the KAM is calculated up to the first neighbor shell with a maximum misorientation angle of 5°. The KAM map serves as a measure of

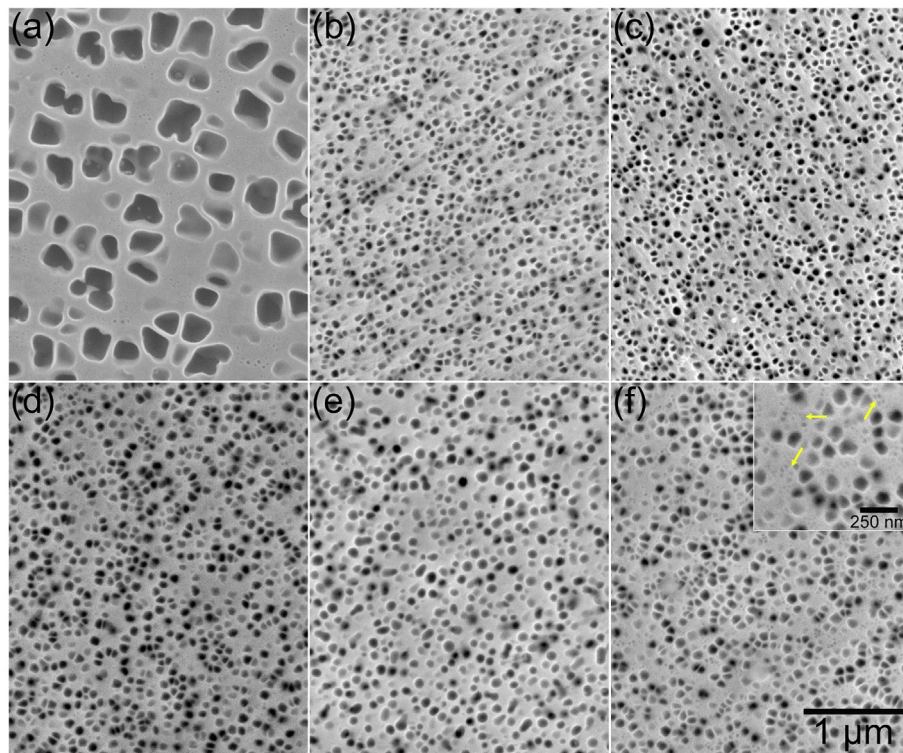


Fig. 4. Secondary electron SEM images showing the features of γ' precipitates for specimens (a) as-HIPed, (b) S, (c) SA1, (d) SA2, (e) SSA1 and (f) SSA2. The insert in (g) is a higher magnification image of specimen SSA2.

the deformation-induced local orientation gradients inside grain, and KAM value is higher in grains whose dislocation density is higher [21]. The unindexed areas (black area) appear due to the severe plastic

deformation at these regions [22], which mainly located in the grain boundaries and small grains (IPF maps in Fig. 7). The KAM maps reveal similar results that KAM values increase at the grain boundaries and

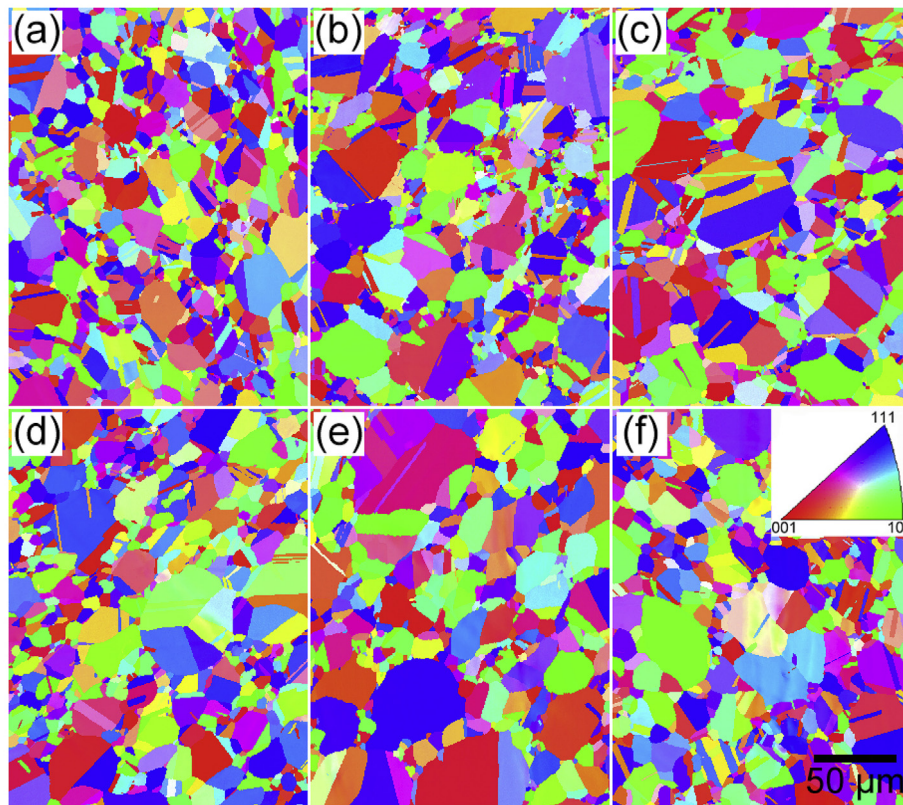


Fig. 5. EBSD IPF maps of (a) as-HIPed, (b) S, (c) SA1, (d) SA2, (e) SSA1 and (f) SSA2 specimens.

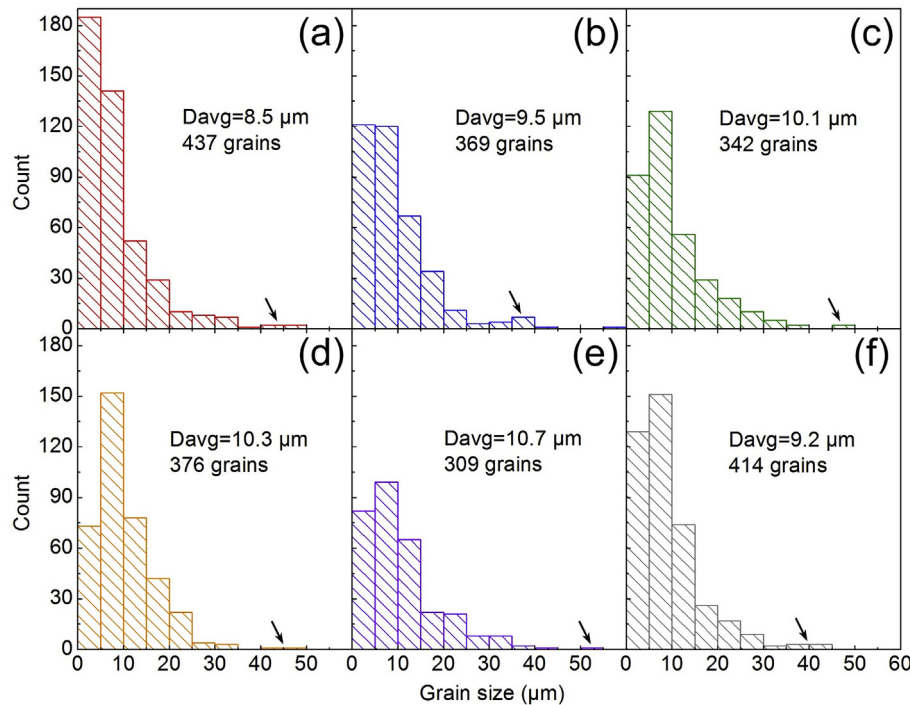


Fig. 6. Grain size distribution of specimens (a) as-HIPed, (b) S, (c) SA1, (d) SA2, (e) SSA1 and (f) SSA2.

small grains. These observations illustrate that the plastic strain and lattice curvature are preferentially accommodated inside the small grains and grain boundaries [21].

3.4. Examination of the fracture surface

Fig. 8 shows the typical fracture morphologies of all the tested specimens. All the specimens failed with a flat fracture surface that is normal to the tensile direction (the insert in Fig. 8) which is believed to be dominated by plane strain condition and suggests poor fracture toughness [23]. From Fig. 8, crack initiation occurs mainly at the site near surface of specimen and then propagates by a transgranular mode leading to the final fracture. In higher magnification images (Fig. 8), the fracture surface is covered with fully dimples suggesting the alloy fractured in a ductile mode [24]. Besides, failure via inter-particle debonding fracture is also observed which is primarily due to the cracking along the remained prior particle boundaries (PPBs) [25], as shown in

Fig. 9. This result reveals that the weakened metallurgical bonding caused by PPBs could be nucleation site and propagation path for cracking and accelerates the failure of the alloy.

4. Discussion

4.1. Corresponding mechanism for microstructure and mechanical performance

4.1.1. The role of solution cooling rate on tuning the size, morphology and size distribution of γ' precipitates

From Fig. 4, the γ' precipitates exhibit different features between as-HIPed specimen and solution treated specimen (S) which are strongly related to the applied cooling approach [9,20]. The HIP process is similar with solution treatment and due to the temperature applied in this work, 1170 °C, is such closer to the solution temperature, thus the difference observed in as-HIP and S specimens can be attributed to the

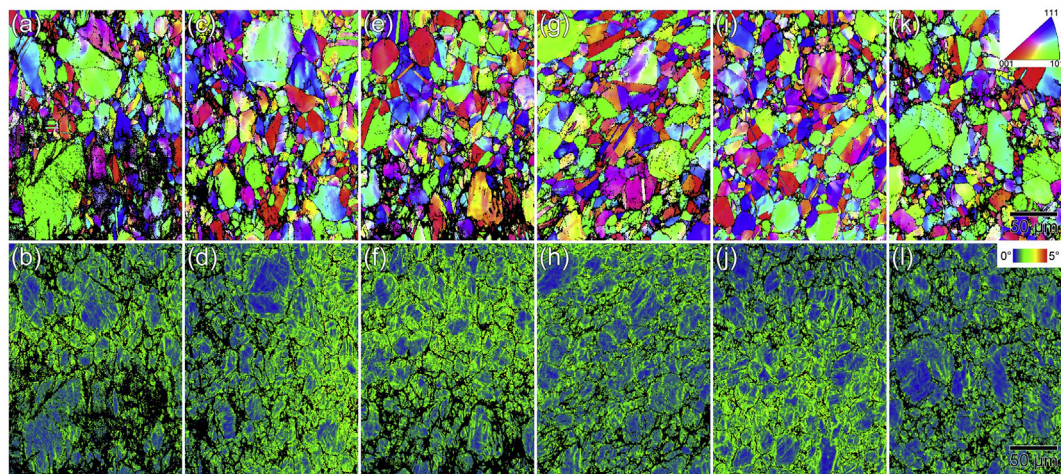


Fig. 7. EBSD (a, c, e, g, i, k) IPF maps and (b, d, f, h, j, l) KAM maps showing microstructural evolution of (a, b) as-HIPed, (c, d) S, (e, f) SA1, (g, h) SA2, (i, j) SSA1 and (k, l) SSA2 specimens during tensile deformation.

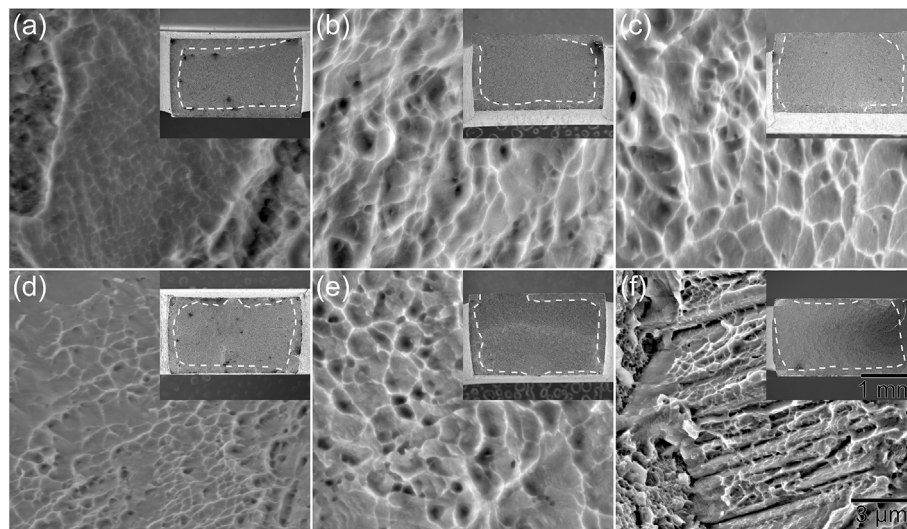


Fig. 8. Secondary electron SEM images showing the fracture surfaces of as-HIPed specimens (a), specimen S (b), SA1 (c), SA2(d), SSA1 (e) and SSA2 (f). The insert is a full view of the fracture surface.

different applied cooling rate reasonably. The as-HIPed specimen was cooled by furnace cooling, i.e., extremely slow cooling rate, after the HIP process. In contrast, a much high cooling rate was used in the specimen S. With the purpose to understand the underlying mechanism, precipitation thermodynamic calculations are performed using the Panprecipitation module in Pandat software under continuous cooling process, in which the cooling rates are set as 1 °C/min and 360 °C/min to simulate the current cases of as-HIPed and S specimens, respectively. In the calculations, the nucleation kinetics of precipitates is inferred from classical nucleation theory (CNT) extended for multicomponent systems [19]. Accordingly, the transient nucleation rate, J , is given by

$$J = N_v Z \beta^* \exp\left(-\frac{\Delta G^*}{R_g T}\right) \exp\left(\frac{-\tau}{t}\right) \quad (1)$$

in which N_v is the nucleation site density, Z is the Zeldovich factor, β^* denotes the atomic attachment rate, R_g is the gas constant, T is the temperature, τ is the incubation time for nucleation and t is the time. And the activation energy for nucleation is calculated from

$$\Delta G^* = \frac{16\pi\sigma^3}{3(\Delta G_v + \Delta G_s)^2} \quad (2)$$

ΔG_v is the chemical driving force per volume for nucleation, ΔG_s is the elastic strain energy per volume of precipitate which is associated with the lattice misfit and σ is the interfacial energy of the γ/γ' interface. For a spherical nucleus,

$$Z = \frac{V_\alpha \Delta G^2}{8\pi \sqrt{\sigma^3 R_g T}} \quad (3)$$

$$\beta^* = \frac{16\pi\sigma^2 D_{eff}}{\Delta G^2 a^4} \quad (4)$$

$$\tau = \frac{8R_g T \sigma a^4}{V_\alpha^2 \Delta G^2 D_{eff}} \quad (5)$$

$$D_{eff} = \left[\sum_{i=1}^n \frac{(C_{pi} - C_{0i})^2}{C_{0i} D_{0i}} \right]^{-1} \quad (6)$$

where V_α is the molar volume of the matrix, a is the lattice constant of γ' , D_{eff} is the effective diffusivity as expressed as Eq. (6). In which C_{pi} and C_{0i} represent the mean concentration in γ' and γ phases, respectively.

Fig. 10 shows the simulation results. For as-HIPed specimen soaked at high temperature (1170 °C) and high pressure (150 MPa) for 4 h, a bimodal distribution consisting of butterfly-shaped secondary γ' with lower number density and small spherical tertiary γ' (**Fig. 4a**) were developed. **Fig. 10a** shows the driving force for nucleation of γ' in this case (black line), the first γ' nucleation burst occurs at higher temperature (compared with the high cooling rate case) as the driving force decreases at higher temperature then these γ' nuclei grow rapidly as a result of diffusion of the γ' forming elements at higher temperature [26] which in turn reduces the supersaturation in matrix leading to the

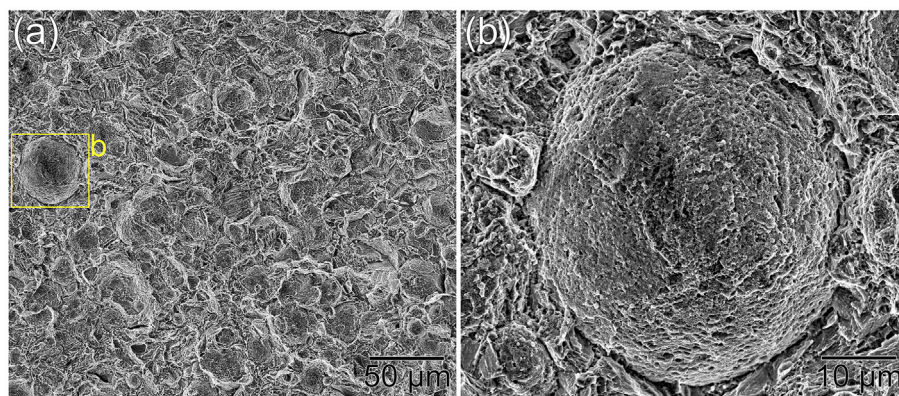


Fig. 9. Fracture surface of the specimen SSA2. (a) a low magnification SEM image, (b) higher magnification images corresponding to the labelled areas b in (a).

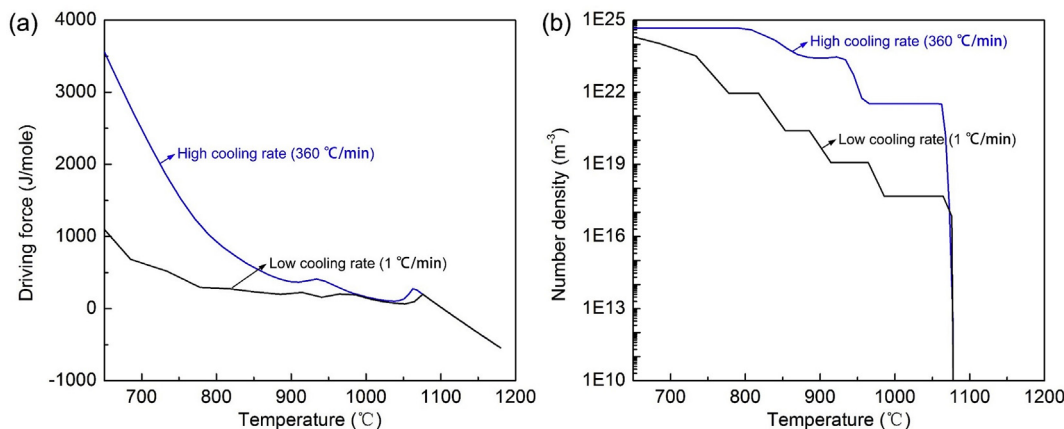


Fig. 10. Calculated (a) driving force for nucleation and (b) number density of γ' precipitates during continuous cooling from 1180 to 650 °C. The as-HIPed specimen was cooled by furnace cooling (slow cooling rate) after the HIP process while the specimen S was air cooled following solution treatment (high cooling rate). Thus, two cooling rates, 1 and 360 °C/min, were applied to simulate the cooling process of as-HIPed and S specimens, respectively. During the solution cooling process with different cooling rate, variational features of γ' precipitates can be obtained.

“shut-off” by soft impingement of the γ' nucleation burst [27]. This is supported by the prediction of driving force, which first increases with decreasing temperature until the γ' nucleation occurs. After that, it fluctuates with cooling process going on and start to increase slowly again below 800 °C as a result of that higher undercooling is available. It leads to the second burst of γ' nucleation and corresponding fine tertiary γ' precipitates (or bimodal distribution of γ') [26,27]. In the case of fast cooling rate (corresponding to the air cooling, specimen S), the driving force shows similar characteristic with that in as-HIPed specimen at the initial stage of first nucleation burst of γ' . However, it increases within a much shorter period and in this context, the shut-off of nucleation may not be activated resulting in the unimodal particle size distribution in this case [28].

The number density of precipitates in these two specimens are also consistent with the calculation results (Fig. 10b). It is obvious that the first nucleation burst of γ' occurs at lower temperature for specimen S under a higher nucleation driving force (Fig. 10a) [29]. Thus, larger nucleation rate of γ' is expected to lead to a higher number density, see Fig. 10b.

Due to the available time at higher temperature is adequate for diffusion of γ' -forming elements, larger size of γ' is observed in as-HIPed specimen compared to specimen S [30,31]. Additionally, the higher number density for γ' limits the distance between individual precipitates, namely, the available solute atoms for growth in fast cooling case (S) is less than that in slow cooling one (as-HIPed specimen) [28]. As a result, the smaller size of γ' is reasonable under these two combined mechanisms.

The developed split γ' precipitates in as-HIPed specimen are also attributed to the larger mobility of γ' -forming elements which produces a large misfit between γ matrix and γ' precipitate [32] leading to anisotropic growth of γ' [33,34].

4.1.2. The evolution of γ' precipitates during SAT and MAT

Fig. 11 shows the corresponding size and volume fraction of secondary γ' under different heat treatments. As discussed in the above section, the much smaller size and slightly decreased volume fraction in γ' for specimen S can be rationalized through much higher cooling rate. The SAT at 760 °C for 8 (specimen SA1, Figs. 4c) and 16 h (specimen SA2, Fig. 4d) result in a larger average size of γ' accompanied with higher volume fraction compared to specimen S indicating growth and coarsening occur during this stage [35]. Both processes are controlled by diffusion mechanism while the supersaturation drives the growth of γ' [31] and surface energy dominates the coarsening of γ' [28]. The tiny fluctuation between specimen SA1 and SA2 may be induced by statistical error. Additionally, the γ' precipitates in these two cases are much

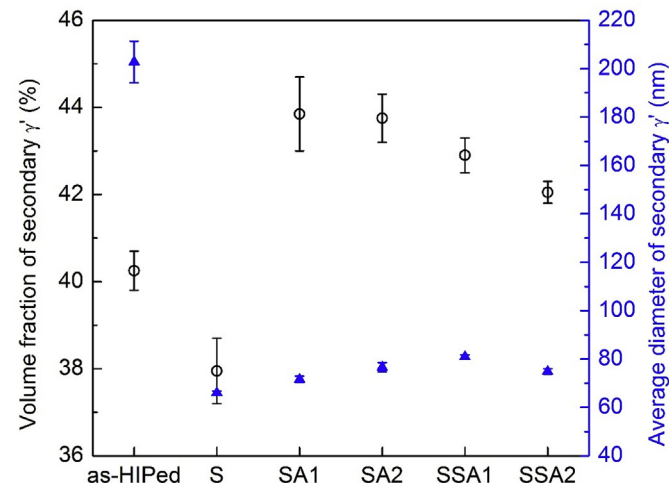


Fig. 11. Variation for average diameter and volume fraction of secondary γ' precipitates up different heat treatments.

closer to the cuboidal morphology and almost no split of γ' precipitates are observed. It implies the fast cooling rate strongly limits the element diffusion process which maintains a moderate misfit between γ and γ' leading to a restricted anisotropic split from spherical or cuboidal morphology [33,34].

When stabilization procedure is applied in MAT, the γ' precipitates exhibit different features compared with the cases of SAT. For the case of specimen SSA1 (stabilized at 980 °C for 1 h), the secondary γ' precipitates display larger size and lower number density than that in SA1 and SA2 specimens. This is due to the fast diffusion rate of alloying elements and lower undercooling at the stabilization temperature (980 °C) [28]. Besides, the supersaturation in matrix is reduced significantly at that higher temperature (980 °C). Similar phenomenon is observed in the specimen SSA2, however, some fine tertiary γ' precipitates emerge in the γ channels between the secondary γ' precipitates (Fig. 4f), which may be related to the slight lower volume fraction of secondary γ' in this case. This phenomenon is attributed to the lower stabilization temperature (650 °C), the γ matrix keeps some supersaturation assisting the nucleation of γ' in the following cooling or aging process to form the tertiary γ' [36], as indicated by yellow arrows in the insert image of Fig. 4f.

4.1.3. Mechanical responses under different heat treatments

The corresponding hardness and tensile strength are strongly related to the γ' precipitates. Extensively investigations [37–39] have been carried out to establish the correlation between the features of γ' precipitates and strength of nickel-based superalloys and provide deep insight on this issue. There is a critical size for γ' precipitates to obtain the maximum strength, while away from (smaller or larger) this critical value will deliver a weakened strengthening effect [1,37,38]. It should be noted that this critical size depends on the specific composition, namely, the optimized size for γ' changes upon different alloys with varied compositions. In contrast, the enlarged volume fraction of γ' precipitates always contributes to the strength positively. Take the consideration of the similar grain size among all the specimens (Fig. 6), it is reasonable to discuss the mechanical responses under different heat treatments based on the variation of γ' precipitates. The lowest strength in as-HIPed specimen is largely attributed to the coarse- γ' precipitates [14] as well as the low volume fraction. When smaller γ' precipitates generated during the solution cooling process in specimen S, a higher strength is achieved in this case. For SAT specimens, the enhanced volume fraction of γ' dominates over the increase size in γ' precipitates resulting in a better mechanical strength than the specimen S accompanied with lower ductility. On one hand, the higher volume fraction of γ' precipitates improve the strength of the alloy, on the other hand, it increases the susceptibility of damage tolerance leading to an inferior ductility [40]. This combined mechanical performance, referred as the strength-ductility trade-off effect, is prevalent in metallic materials [41]. It is interesting that higher total elongation is observed in SA2 specimen compared with SA1, which may imply that coarse- γ' precipitates can recover some ductility in precipitate-strengthened nickel-based superalloys. Stabilized at high temperature with a short time (980 °C/1 h, specimen SSA1) slightly decreases the strength while its elongation is maintained compared with specimen SA2. This combined performance can be attributed to the larger size of γ' precipitates in this condition. Coarse- γ' precipitates generate negative effect in strengthening the alloy while benefit the ductility at the same time. This result supports the above hypothesis that the high ductility is related to larger γ' precipitates. The most excellent property, i.e. the highest tensile strength and an acceptable elongation, is achieved in specimen SSA2 which suffered a lower temperature stabilization process (650 °C/24 h) prior to aging. Compared its γ' precipitates feature with that in specimen SSA1, the higher strength should be attributed to the combination of smaller size of secondary γ' (Fig. 11) and emergence of tertiary γ' in the channel between secondary γ' (Fig. 4f) [30]. These above results show the advantage of stabilization process (low temperature and long time) in helping the alloy reach an excellent tensile property at room temperature.

4.2. Relationship between Vickers hardness and tensile strength of nickel-based superalloys

It is unambiguous that Vickers hardness is positively related to the tensile strength for nickel-based superalloys and other metallic materials [42]. Jackson et al. [5] reported that the hardness correlates better with the ultimate tensile strength rather than the yield strength from the perspective of indentation induced strain. However, based on numerous experimental results, a more linear relationship has been observed between Vickers hardness and yield strength in structural materials [3]. In this work, we examine these relations using the data both from our work and literature [3,5,43,44]. It should be noted that only the results of nickel alloys and nickel-based superalloys are considered in the current discussion. The corresponding outcomes are plotted in Fig. 12. Using linear fitting method, the quantitative relations are described by the following equations,

$$\sigma_{YS} = 2.34H_v \quad (7)$$

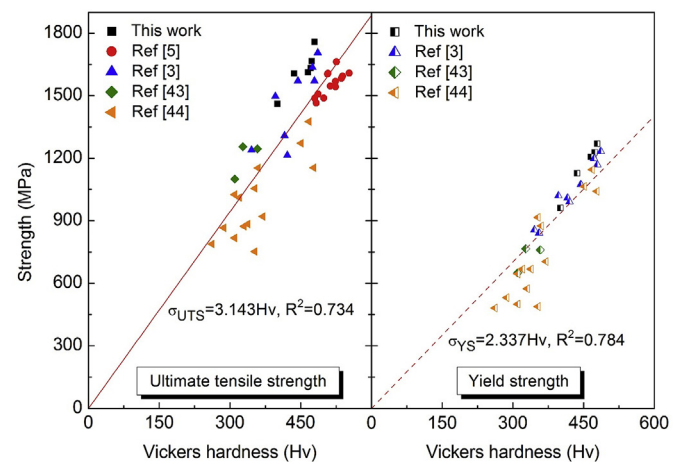


Fig. 12. Relationship between tensile strength and Vickers hardness.

$$\sigma_{UTS} = 3.14H_v \quad (8)$$

where σ_{YS} and σ_{UTS} represent the yield strength and ultimate tensile strength, respectively. H_v is the value of Vickers hardness. From Fig. 12, both points of the ultimate tensile strength and yield strength are located near the fitted line with moderate deviation. However, a little higher correlation coefficient (R^2) for yield strength vs Vickers hardness is observed. It should be attributed to the different work hardening effect in different specimens under variation plastic strains (15%–24% engineering tensile strain) [5]. It seems that the Vickers hardness has a better proportional relationship with yield strength from the view of correlation coefficient. However, using Vickers hardness to assess the ultimate tensile strength via Eq. (8) is also acceptable. By these above relationships, the tensile strength of nickel-based superalloys or the influence of alloy element/grain size/ γ' precipitate features/heat treatment procedures on the tensile property can be rapidly assessed.

5. Conclusions

1. Different aging treatments are applied to a prototypical PM nickel-based superalloy and the two-step aging, namely, stabilized at 650 °C for 24 h followed by aged at 760 °C for 16 h, can make the alloy achieve the highest hardness, tensile strength and an acceptable ductility at room temperature.
2. The solution cooling rate plays an important role in tailoring the morphology, size and size distribution of γ' precipitates which is clarified by the precipitation calculation enabled by multi-component thermodynamic database.
3. Stabilization at high temperature (980 °C for 1 h) before aging leads to a coarsening of γ' precipitates, which in turn results a lower corresponding tensile strength than the case of single aging treated or stabilized at low temperature.
4. All the specimens fracture mainly in a transgranular ductile mode at room temperature tensile test. Besides, the PPBs act as weakened interfaces could be initial sites for cracking nucleation and propagation resulting in earlier fracture of the material.
5. Vickers hardness is examined has a linear relationship with both ultimate tensile strength and yield strength which is helpful in rapidly assessing the strength of a nickel-based superalloy with different microstructures.

Acknowledgement

This work was supported by the National Key Research and Development Program of China (2016YFB0700300). And H. W. appreciates the financial support from the outstanding graduate project of Advanced Non-ferrous Metal Structural Materials and Manufacturing

Collaborative Innovation Center.

References

- [1] R.C. Reed, The Superalloys: Fundamentals and Applications, Cambridge university press, Cambridge, UK, 2008.
- [2] T.M. Pollock, S. Tin, Nickel-based superalloys for advanced turbine engines: chemistry, microstructure, and properties, *J. Propuls. Power* 22 (2) (2006) 361–374.
- [3] T. Osada, Y. Gu, N. Nagashima, Y. Yuan, T. Yokokawa, H. Harada, Optimum microstructure combination for maximizing tensile strength in a polycrystalline superalloy with a two-phase structure, *Acta Mater.* 61 (5) (2013) 1820–1829.
- [4] H.Y. Li, J.F. Sun, M.C. Hardy, H.E. Evans, S.J. Williams, T.J.A. Doel, P. Bowen, Effects of microstructure on high temperature dwell fatigue crack growth in a coarse grain PM nickel based superalloy, *Acta Mater.* 90 (2015) [355]–[369].
- [5] M.P. Jackson, R.C. Reed, Heat treatment of UDIMET 720Li: the effect of microstructure on properties, *Mater. Sci. Eng., A* 259 (1) (1999) 85–97.
- [6] D.M. Collins, B.D. Conduit, H.J. Stone H J, M.C. Hardy, G.J. Conduit, R.J. Mitchell, Grain growth behavior during near- γ' solvus thermal exposures in a polycrystalline nickel-base superalloy, *Acta Mater.* 61 (9) (2013) 3378–3391.
- [7] J.Y. Hwang, S. Nag, A.R.P. Singh, R. Srinivasan, J. Tiley, G.B. Viswanathan, H.L. Fraser, R. Banerjee, Compositional variations between different generations of γ' precipitates forming during continuous cooling of a commercial nickel-base superalloy, *Metall. Mater. Trans.* 40 (13) (2009) 3059–3068.
- [8] Y.Q. Chen, E. Francis, J. Robson, M. Preuss, S.J. Haigh, Compositional variations for small-scale gamma prime (γ') precipitates formed at different cooling rates in an advanced Ni-based superalloy, *Acta Mater.* 85 (2015) 199–206.
- [9] J. Tiley, G.B. Viswanathan, R. Srinivasan, R. Banerjee, D.M. Dimiduk, H.L. Fraser, Coarsening kinetics of γ' precipitates in the commercial nickel base Superalloy René 88 DT, *Acta Mater.* 57 (8) (2009) 2538–2549.
- [10] M. Zhang, G.Q. Liu, H. Wang, B.F. Hu, Stability of γ' multimodal microstructure in a Ni-based powder metallurgy superalloy, *Sci. China Technol. Sci.* 61 (2018) 1824–1828 <https://doi.org/10.1007/s11431-018-9372-8>.
- [11] H. Wu, Z. Huang, N. Zhou, J. Chen, P. Zhou, L. Jiang, A study of solution cooling rate on γ' precipitate and hardness of a polycrystalline Ni-based superalloy using a high-throughput methodology, *Mater. Sci. Eng.* 739 (2019) 473–479.
- [12] R.S. Moshtaghi, S.I.R.O.U.S. Asgari, Growth kinetics of γ' precipitates in superalloy IN-738LC during long term aging, *Mater. Des.* 24 (5) (2003) 325–330.
- [13] C.L. Jia, C.C. Ge, Q.Z. Yan, Microstructure evolution and mechanical properties of disk superalloy under multiplex heat treatment, *Mater. Sci. Eng., A* 659 (2016) 287–294.
- [14] R.W. Kozar, A. Suzuki, W.W. Milligan, J.J. Schirra, M.F. Savage, T.M. Pollock, Strengthening mechanisms in polycrystalline multimodal nickel-base superalloys, *Metall. Mater. Trans.* 40 (7) (2009) 1588–1603.
- [15] J.R. Vaunois, J. Cormier, P. Villechaise, A. Devaux, B. Flagelet, Influence of Both γ' Distribution and Grain Size on the Tensile Properties of UDIMET 720Li at Room temperature[C]//7th International Symposium on Superalloys 718 and Derivatives, (2010), pp. 199–213.
- [16] D.D. Krueger, R.D. Kissinger, R.G. Menzies, C.S. Wukusick, Fatigue crack growth resistant nickel-base article and alloy and method for making, U.S. Patent, 4,957,567, (1990).
- [17] L. Jiang, H. Wang, P.K. Liaw, C.R. Brooks, D.L. Klarstrom, Characterization of the temperature evolution during high-cycle fatigue of the ULTIMET superalloy: experiment and theoretical modeling, *Metall. Mater. Trans.* 32 (9) (2001) 2279–2296.
- [18] M. Pinz, G. Weber, W.C. Lenthe, M.D. Uchic, T.M. Pollock, S. Ghosh, Microstructure and property based statistically equivalent RVEs for intragranular γ – γ' microstructures of Ni-based superalloys, *Acta Mater.* 157 (2018) 245–258.
- [19] W. Cao, S.-L. Chen, F. Zhang, K. Wu, Y.A. Chang, R. Schmid-Fetzer, W.A. Oates, PANDAT software with PanEngine, PanOptimizer and PanPrecipitation for multi-component phase diagram calculation and materials property simulation, *Calphad* 33 (2) (2009) 328–342.
- [20] A.R.P. Singh, S. Nag, S. Chattopadhyay, Y. Ren, J. Tiley, G.B. Viswanathan, H.L. Fraser, R. Banerjee, Mechanisms related to different generations of γ' precipitation during continuous cooling of a nickel base superalloy, *Acta Mater.* 61 (1) (2013) 280–293.
- [21] Z. Li, C.C. Tasan, K.G. Pradeep, D. Raabe, A TRIP-assisted dual-phase high-entropy alloy: grain size and phase fraction effects on deformation behavior, *Acta Mater.* 131 (2017) 323–335.
- [22] M.J. Yao, K.G. Pradeep, C.C. Tasan, D. Raabe, A novel, single phase, non-equiautomic FeMnNiCoCr high-entropy alloy with exceptional phase stability and tensile ductility, *Scripta Mater.* 72 (2014) 5–8.
- [23] J.W. Hutchinson, Singular behaviour at the end of a tensile crack in a hardening material, *J. Mech. Phys. Solids* 16 (1) (1968) 13–31.
- [24] Z. Li, D. Raabe, Influence of compositional inhomogeneity on mechanical behavior of an interstitial dual-phase high-entropy alloy, *Mater. Chem. Phys.* 210 (2018) 29–36.
- [25] G.A. Rao, M. Kumar, M. Srinivas, D.S. Sarma, Effect of standard heat treatment on the microstructure and mechanical properties of hot isostatically pressed superalloy inconel 718, *Mater. Sci. Eng., A* 355 (1–2) (2003) 114–125.
- [26] P.M. Sarosi, B. Wang, J.P. Simmons, Y. Wang, M.J. Mills, Formation of multimodal size distributions of γ' in a nickel-base superalloy during interrupted continuous cooling, *Scripta Mater.* 57 (8) (2007) 767–770.
- [27] Y.H. Wen, J.P. Simmons, C. Shen, C. Woodward, Y. Wang, Phase-field modeling of bimodal particle size distributions during continuous cooling, *Acta Mater.* 51 (4) (2003) 1123–1132.
- [28] R. Radis, M. Schaffer, M. Albu, G. Kothleitner, P. Pölt, E. Kozeschnik, Multimodal size distributions of γ' precipitates during continuous cooling of UDIMET 720 Li, *Acta Mater.* 57 (2009) 5739–5747.
- [29] S.S. Babu, M.K. Miller, J.M. Vitek, S.A. David, Characterization of the microstructure evolution in a nickel base superalloy during continuous cooling conditions, *Acta Mater.* 49 (20) (2001) 4149–4160.
- [30] H. Wu, J. Li, F. Liu, L. Huang, X. Zeng, Q. Fang, Z. Huang, L. Jiang, A high-throughput methodology search for the optimum cooling rate in an advanced polycrystalline nickel base superalloy, *Mater. Des.* 128 (2017) 176–181.
- [31] Q. Chen, J. Jeppsson, J. Ågren, Analytical treatment of diffusion during precipitate growth in multicomponent systems, *Acta Mater.* 56 (8) (2008) 1890–1896.
- [32] J.S. Van Sluytman, T.M. Pollock, Optimal precipitate shapes in nickel-base γ – γ' alloys, *Acta Mater.* 60 (4) (2012) 1771–1783.
- [33] Y. Chen, T.J.A. Slater, M. Bai, R. Mitchell, O. Ciucia, M. Preuss, S.J. Haigh, An investigation of diffusion-mediated cyclic coarsening and reversal coarsening in an advanced Ni-based superalloy, *Acta Mater.* 110 (2016) 295–305.
- [34] X. Fan, Z. Guo, X. Wang, J. Yang, J. Zou, Morphology evolution of γ' precipitates in a powder metallurgy Ni-base superalloy, *Mater. Char.* 139 (2018) 382–389.
- [35] A.J. Goodfellow, E.I. Galindo-Navia, K.A. Christofidou, N.G. Jones, T. Martin, P.A.J. Bagot, C.D. Boyer, M.C. Hardy, H.J. Stone, Gamma prime precipitate evolution during aging of a model nickel-based superalloy, *Metall. Mater. Trans.* 49 (3) (2018) 718–728.
- [36] A.R.P. Singh, S. Nag, J.Y. Hwang, G.B. Viswanathan, J. Tiley, R. Srinivasan, H.L. Fraser, R. Banerjee, Influence of cooling rate on the development of multiple generations of γ' precipitates in a commercial nickel base superalloy, *Mater. Char.* 62 (9) (2011) 878–886.
- [37] D.M. Collins, H.J. Stone, A modelling approach to yield strength optimisation in a nickel-base superalloy, *Int. J. Plast.* 54 (2014) 96–112.
- [38] E.I. Galindo-Navia, L.D. Connor, C.M.F. Rae, On the prediction of the yield stress of unimodal and multimodal γ' Nickel-base superalloys, *Acta Mater.* 98 (2015) 377–390.
- [39] Q. Fang, L. Li, J. Li, H. Wu, Z. Huang, B. Liu, Y. Liu, P.K. Liaw, A statistical theory of probability-dependent precipitation strengthening in metals and alloys, *J. Mech. Phys. Solids* 122 (2019) 177–189.
- [40] T. Yang, Y.L. Zhao, Y. Tong, Z.B. Jiao, J. Wei, J.X. Cai, X.D. Han, D. Chen, A. Hu, J.J. Kai, K. Lu, Y. Liu, C.T. Liu, Multicomponent intermetallic nanoparticles and superb mechanical behaviors of complex alloys, *Science* 362 (6417) (2018) 933–937.
- [41] Z. Li, K.G. Pradeep, Y. Deng, D. Raabe, C.C. Tasan, Metastable high-entropy dual-phase alloys overcome the strength–ductility trade-off, *Nature* 534 (7606) (2016) 227–230.
- [42] T. Osada, N. Nagashima, Y. Gu, Y. Yuan, T. Yokokawa, H. Harada, Factors contributing to the strength of a polycrystalline nickel–cobalt base superalloy, *Scripta Mater.* 64 (9) (2011) 892–895.
- [43] C. Joseph, C. Persson, M.H. Colliander, Influence of heat treatment on the microstructure and tensile properties of Ni-base superalloy Haynes 282, *Mater. Sci. Eng., A* 679 (2017) 520–530.
- [44] V.A. Popovich, E.V. Borisov, A.A. Popovich, V.S. Sufiakov, D.V. Masaylo, L. Alzina, Impact of heat treatment on mechanical behaviour of Inconel 718 processed with tailored microstructure by selective laser melting, *Mater. Des.* 131 (2017) 12–22.